Light modulation in planar aligned short-pitch deformed-helix ferroelectric liquid crystals

Svetlana P. Kotova,[1,2,*] Sergey A. Samagin,[1,†] Evgeny P. Pozhidaev,[1,3,‡] and Alexei D. Kiselev[3,4,§]

[1]*Lebedev Physical Institute, Leninsky Prospekt 53, 119991 Moscow, Russia*

[2]*Samara State Aerospace University, Moskovskoe Shosse 34, 443086 Samara, Russia*

[3]*Hong Kong University of Science and Technology, Clear Water Bay, 999077 Kowloon, Hong Kong*

[4]*Saint Petersburg National Research University of Information Technologies, Mechanics and Optics, Kronverskyi Prospekt 49, 197101 St. Petersburg, Russia*

(Received 20 August 2015; published 1 December 2015)

We study both experimentally and theoretically modulation of light in a planar aligned deformed-helix ferroelectric liquid crystal (DHFLC) cell with subwavelength helix pitch, which is also known as a short-pitch DHFLC. In our experiments, the azimuthal angle of the in-plane optical axis and electrically controlled parts of the principal in-plane refractive indices are measured as a function of voltage applied across the cell. Theoretical results giving the effective optical tensor of a short-pitch DHFLC expressed in terms of the smectic tilt angle and the refractive indices of the ferroelectric liquid crystal (FLC) are used to fit the experimental data. The optical anisotropy of the FLC material is found to be weakly biaxial. For both the transmissive and reflective modes, the results of fitting are applied to model the phase and amplitude modulation of light in the DHFLC cell. We demonstrate that if the thickness of the DHFLC layer is about 50 μm, the detrimental effect of field-induced rotation of the in-plane optical axes on the characteristics of an axicon designed using the DHFLC spatial light modulator in the reflective mode is negligible.

DOI: 10.1103/PhysRevE.92.062502 PACS number(s): 61.30.Gd, 78.20.Jq, 42.70.Df, 42.79.Kr

I. INTRODUCTION

High-speed, low-power-consuming light modulation is in high demand for a variety of photonic devices used as building blocks of displays and optical information processors. These include tunable lenses, focusers, wave-front correctors, and correlators [1–6].

Usually for such devices, in addition to fast switching times, it is of crucial importance to have a 2π modulation so that the phase can be smoothly tuned from zero to 2π. Liquid crystal (LC) spatial light modulators (SLMs) are widely used as devices to modulate amplitude, phase, or polarization of light waves in space and time [7]. In LC SLMs, nematic liquid crystals are among the most popular LC phases. However, nematic LCs are known to have slow response time and, in addition, this slow response gets worse if the LC layer thickness increases in order to obtain the 2π phase modulation. Therefore, much effort is currently being put forth to optimize the various LC electro-optical modes for the high-speed light modulation.

Ferroelectric liquid crystals (FLCs) represent an alternative and promising chiral liquid crystal material that is characterized by a very fast response time (a detailed description of FLCs can be found, e.g., in Refs. [8,9]). Equilibrium orientational structures in FLCs can be described as helical twisting patterns where FLC molecules align on average along a local unit director

$$\hat{\mathbf{d}} = \cos\theta\hat{\mathbf{h}} + \sin\theta\hat{\mathbf{c}}, \tag{1}$$

where θ is the smectic tilt angle, $\hat{\mathbf{h}}$ is the twisting axis normal to the smectic layers, and $\hat{\mathbf{c}} \perp \hat{\mathbf{h}}$ is the c director. The FLC director (1) lies on the smectic cone depicted in Fig. 1(a) with the smectic tilt angle θ and rotates in a helical fashion about a uniform twisting axis $\hat{\mathbf{h}}$ forming the FLC helix with the helix pitch P. This rotation is described by the azimuthal angle around the cone Φ that specifies orientation of the c director in the plane perpendicular to $\hat{\mathbf{h}}$ and depends on the dimensionless coordinate along the twisting axis

$$\phi = 2\pi(\hat{\mathbf{h}}\cdot\mathbf{r})/P = qx, \tag{2}$$

where $q = 2\pi/P$ is the helix twist wave number.

Figure 1 illustrates the important case of a uniform lying FLC helix in the slab geometry with the smectic layers normal to the substrates and

$$\hat{\mathbf{h}} = \hat{\mathbf{x}}, \quad \hat{\mathbf{c}} = \cos\Phi\hat{\mathbf{y}} + \sin\Phi\hat{\mathbf{z}}, \quad \mathbf{E} = E\hat{\mathbf{z}}, \tag{3}$$

where $\mathbf{E}$ is the applied electric field that is linearly coupled to the spontaneous ferroelectric polarization

$$\mathbf{P}_s = P_s\hat{\mathbf{p}}, \quad \hat{\mathbf{p}} = \hat{\mathbf{h}}\times\hat{\mathbf{c}} = \cos\Phi\hat{\mathbf{z}} - \sin\Phi\hat{\mathbf{y}}, \tag{4}$$

where $\hat{\mathbf{p}}$ is the polarization unit vector. This is the geometry of surface-stabilized FLCs (SSFLCs) pioneered by Clark and Lagerwall in Ref. [10] where they studied electro-optic response of FLC cells confined between two parallel plates subject to homogeneous boundary conditions and made thin enough to suppress the bulk FLC helix. Figure 1(b) also describes the geometry of deformed-helix FLCs (DHFLCs) as it was originally introduced in [11]. The approach to light modulation that uses the electro-optical properties of helical structures in DHFLCs with subwavelength pitch also known as the short-pitch DHFLCs will be of our primary concern.

In short-pitch DHFLC cells, the FLC helix is characterized by a submicron helix pitch $P < 1$ μm and a relatively large tilt angle $\theta > 30^\circ$. The electro-optical response of DHFLC

*kotova@fian.smr.ru
†samagin@fian.smr.ru
‡epozhidaev@mail.ru
§alexei.d.kiselev@gmail.com

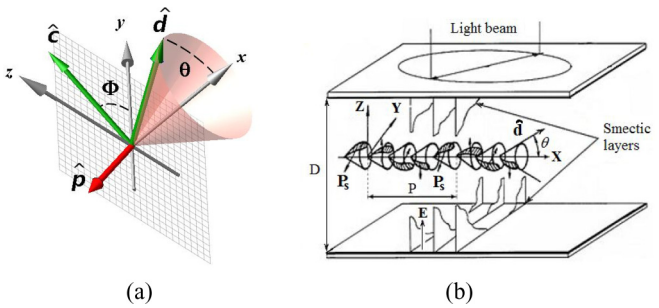

(a) (b)

FIG. 1. (Color online) Geometry of (a) a smectic cone and (b) a planar aligned FLC cell with a uniform lying helix.

cells exhibits a number of peculiarities that make them useful for LC devices such as high-speed spatial light modulators [12–16], color-sequential liquid crystal display cells [17], and optic fiber sensors [18,19]. The effects caused by electric-field-induced distortions of the helical structure underline the mode of operation of such cells. In a typical experimental setup, these effects are probed by performing measurements of the transmittance of normally incident light through a cell placed between crossed polarizers.

In this article our goal is to examine light modulation in planar aligned short-pitch DHFLC (PADHFLC) cells with a uniform lying FLC helix (the twisting axis is parallel to the substrates) and the related physical characteristics. This is the case that was studied theoretically in Refs. [20,21] where the transfer matrix approach to polarization gratings was employed to define the effective dielectric tensor of short-pitch DHFLCs. In particular, it was found that, in contrast to the case of vertically aligned DHFLCs [15,16], the in-plane optical axes of PADHFLCs sweep in the plane of the cell under the action of the applied electric field, thus producing changes in the polarization state of the incident light. More generally, the biaxial anisotropy and rotation of the optical axes induced by the electric field in short-pitch DHFLC cells can be interpreted as the orientational Kerr effect [15,16,21].

For a detailed experimental characterization of this effect, we employ the experimental technique based on the Mach-Zehnder interferometer that goes beyond the limitations of the above mentioned standard experimental procedure and provides additional information on the principal refractive indices. Then we use the results as input parameters to study light modulation in the DHFLC cell operating in both the transmissive and reflective modes. Our investigation into the effects of amplitude modulation is based on the results of modeling of an axicon designed using the DHFLC spatial light modulator in the reflective mode.

The axicon as a cylindrically symmetric optical element that transforms an incident plane wave into a narrow beam of light along the optical axis has a long history dating back to the papers by McLeod [22,23]. Laser beams propagating through axicons have two significant properties: (a) They generate a line focus, where the on-axis intensity stays high over much longer distances compared to focusing by conventional lenses, and (b) they generate ringlike intensity profiles in the far field. Both of these properties proved useful in many applications such as atom guiding and trapping [24], annular focusing in laser machining [25], generation of quasinondiffracting Bessel-like beams [26–28], subdiffraction limit imaging [29], and optical micromanipulation [30–32].

The layout of the paper is as follows. In Sec. II we introduce our notation, describe the recent theoretical results [21] on the effective optical tensor of short-pitch biaxial FLCs, and discuss the orientational Kerr effect. Experimental details are given in Sec. III, where we describe the samples and the setup employed to perform measurements. The experimental data are fitted using the expression for the effective optical tensor. Section IV deals with modulation of light in the DHFLC cells in both transmissive and reflective modes. Experimental results are used to compute the amplitudes and phases of the components of transmitted and reflected light waves. Deformed-helix FLC spatial light modulator acting as an axicon is modeled as a two-dimensional (2D) array of pixels which are DHFLC cells. In order to study the effects of amplitude modulation, the intensity distribution in the focal plane of the axicon is evaluated for both DHFLC and ideal (no amplitude modulation) axicons. In Sec. V we discuss the results and summarize. Technical results are relegated to Appendixes.

II. ORIENTATIONAL KERR EFFECT

In this section we introduce notation and briefly discuss the electro-optical properties of short-pitch DHFLC cells described by the effective dielectric (optical) tensor $\boldsymbol{\varepsilon}_{\text{eff}}$ defined in terms of averages over the distorted FLC helical structure [20] (see Appendix A). For the geometry of a uniform lying FLC helix [see Fig. 1(b)], we recapitulate the analytical results for the optical tensor of a biaxial ferroelectric liquid crystal with subwavelength pitch [21]. In the subsequent section these results will be used to interpret the experimental data.

We consider a FLC layer of thickness D with the z axis which, as is indicated in Fig. 1, is normal to the bounding surfaces $z = 0$ and $z = D$ and introduce the effective dielectric tensor $\boldsymbol{\varepsilon}_{\text{eff}}$ describing a homogenized DHFLC helical structure.

For a biaxial FLC, the components of the dielectric tensor $\boldsymbol{\varepsilon}$ are given by

$$\begin{aligned}\epsilon_{ij} &= \epsilon_\perp \delta_{ij} + (\epsilon_1 - \epsilon_\perp) d_i d_j + (\epsilon_2 - \epsilon_\perp) p_i p_j \\ &= \epsilon_\perp (\delta_{ij} + u_1 d_i d_j + u_2 p_i p_j), \end{aligned} \tag{5}$$

where $i, j \in \{x, y, z\}$, δ_{ij} is the Kronecker symbol, d_i (p_i) is the ith component of the FLC director (unit polarization vector) given by Eq. (1) [Eq. (4)], $u_i = (\epsilon_i - \epsilon_\perp)/\epsilon_\perp = \Delta\epsilon_i/\epsilon_\perp = r_i - 1$ are the anisotropy parameters, and $r_1 = \epsilon_1/\epsilon_\perp$ ($r_2 = \epsilon_2/\epsilon_\perp$) is the anisotropy (biaxiality) ratio. Note that, in the case of uniaxial anisotropy with $u_2 = 0$, the principal values of the dielectric tensor are $\epsilon_2 = \epsilon_\perp$ and $\epsilon_1 = \epsilon_\parallel$, where $n_\perp = \sqrt{\mu\epsilon_\perp}$ ($n_\parallel = \sqrt{\mu\epsilon_\parallel}$) is the ordinary (extraordinary) refractive index and the magnetic tensor of the FLC is assumed to be isotropic with the magnetic permittivity μ. We also assume that the medium surrounding the layer is optically isotropic and is characterized by the dielectric constant ϵ_{m}, the magnetic permittivity μ_{m}, and the refractive index $n_{\text{m}} = \sqrt{\mu_{\text{m}}\epsilon_{\text{m}}}$.

Assuming that the pitch to wavelength ratio P/λ is sufficiently small, the effective dielectric tensor can be expressed in terms of the averages over the pitch of the distorted FLC helical structure. Explicit formulas for the components of the tensor

are given in Appendix A. These formulas can be used to derive the effective optical tensor of the homogenized short-pitch DHFLC cell for both vertically and planar aligned FLC helices [15,21].

We concentrate on the geometry of the planar aligned DHFLC helix shown in Fig. 1(b). For this geometry, the effective dielectric tensor can be written in the following form [21]:

$$\boldsymbol{\varepsilon}_{\text{eff}} = \begin{pmatrix} \epsilon_h + \gamma_{xx}\alpha_E^2 & \gamma_{xy}\alpha_E & 0 \\ \gamma_{xy}\alpha_E & \epsilon_p + \gamma_{yy}\alpha_E^2 & 0 \\ 0 & 0 & \epsilon_p - \gamma_{yy}\alpha_E^2 \end{pmatrix}, \quad (6)$$

where, following Ref. [15], we have introduced the electric-field parameter

$$\alpha_E = \chi_E E/P_s \quad (7)$$

proportional to the dielectric susceptibility of the Goldstone mode [33,34]: $\chi_E = \partial\langle P_z\rangle/\partial E$ with $P_z = P_s\cos\Phi$.

The zero-field dielectric constants ϵ_h and ϵ_p that enter the tensor (6) are given by

$$\epsilon_h/\epsilon_\perp = (n_h/n_\perp)^2 = r_2^{-1/2}\left\{\sqrt{r_2} + u_1\cos^2\theta\left(\frac{r_2-1}{\sqrt{u}+\sqrt{r_2}} + u^{-1/2}\right)\right\}, \quad (8a)$$

$$\epsilon_p/\epsilon_\perp = (n_p/n_\perp)^2 = \sqrt{r_2 u}, \quad (8b)$$

$$u = u_1\sin^2\theta + 1. \quad (8c)$$

Similar results for the coupling coefficients γ_{xx}, γ_{yy}, and γ_{xy} read

$$\gamma_{xx}/\epsilon_\perp = \frac{3\sqrt{r_2/u}}{(\sqrt{u}+\sqrt{r_2})^2}(u_1\cos\theta\sin\theta)^2, \quad (9a)$$

$$\gamma_{yy}/\epsilon_\perp = \frac{3\sqrt{r_2 u}}{(\sqrt{u}+\sqrt{r_2})^2}(u - r_2), \quad (9b)$$

$$\gamma_{xy}/\epsilon_\perp = \frac{2\sqrt{r_2}}{\sqrt{u}+\sqrt{r_2}}u_1\cos\theta\sin\theta. \quad (9c)$$

Note that the simplest averaging procedure previously used in Refs. [12,15,20] heavily relies on the first-order approximation where the director distortions are described by the term linearly proportional to the electric field. Quantitatively, the difficulty with this approach is that the linear approximation may not suffice for accurate computing of the second-order contributions to the diagonal elements of the dielectric tensor (6). In Ref. [21] the results (6)–(9c) were derived by using the modified averaging technique that allows high-order corrections to the dielectric tensor to be accurately estimated and improves agreement between the theory and the experimental data in the high-field region.

The dielectric tensor (6) is characterized by the three generally different principal values (eigenvalues) and the corresponding optical axes (eigenvectors) as follows:

$$\boldsymbol{\varepsilon}_{\text{eff}} = \epsilon_z\hat{\mathbf{z}}\otimes\hat{\mathbf{z}} + \epsilon_+\hat{\mathbf{d}}_+\otimes\hat{\mathbf{d}}_+ + \epsilon_-\hat{\mathbf{d}}_-\otimes\hat{\mathbf{d}}_-, \quad (10)$$

$$\epsilon_z = n_z^2 = \epsilon_{zz}^{(\text{eff})} = \epsilon_p - \gamma_{yy}\alpha_E^2, \quad (11)$$

$$\epsilon_\pm = n_\pm^2 = \bar{\epsilon} \pm \sqrt{[\Delta\epsilon]^2 + [\gamma_{xy}\alpha_E]^2}, \quad (12)$$

where

$$\bar{\epsilon} = \left(\epsilon_{xx}^{(\text{eff})} + \epsilon_{yy}^{(\text{eff})}\right)/2 = \bar{\epsilon}_0 + (\gamma_{xx}+\gamma_{yy})\alpha_E^2/2, \quad (13)$$

$$\Delta\epsilon = \left(\epsilon_{xx}^{(\text{eff})} - \epsilon_{yy}^{(\text{eff})}\right)/2 = \Delta\epsilon_0 + (\gamma_{xx}-\gamma_{yy})\alpha_E^2/2, \quad (14)$$

$$\bar{\epsilon}_0 = (\epsilon_h+\epsilon_p)/2,\ \Delta\epsilon_0 = (\epsilon_h-\epsilon_p)/2. \quad (15)$$

The in-plane optical axes are given by

$$\hat{\mathbf{d}}_+ = \cos\psi_d\hat{\mathbf{x}} + \sin\psi_d\hat{\mathbf{y}},\quad \hat{\mathbf{d}}_- = \hat{\mathbf{z}}\times\hat{\mathbf{d}}_+, \quad (16)$$

$$2\psi_d = \arg[\Delta\epsilon + i\gamma_{xy}\alpha_E]. \quad (17)$$

From Eq. (6) it is clear that the zero-field dielectric tensor is uniaxially anisotropic with the optical axis directed along the twisting axis $\hat{\mathbf{h}} = \hat{\mathbf{x}}$. The applied electric field changes the principal values [see Eqs. (11) and (12)] so that the electric-field-induced anisotropy is generally biaxial. In addition, the in-plane principal optical axes are rotated about the vector of electric field $\mathbf{E}\parallel\hat{\mathbf{z}}$ by the angle ψ_d given in Eq. (17).

In the low-electric-field region, the electrically induced part of the principal values is typically dominated by the Kerr-like nonlinear terms proportional to E^2,

$$n_+ \approx n_h + \frac{1}{2n_h}\left\{\gamma_{xx} + \frac{\gamma_{xy}^2}{n_h^2-n_p^2}\right\}\alpha_E^2, \quad (18a)$$

$$n_- \approx n_p + \frac{1}{2n_p}\left\{\gamma_{yy} - \frac{\gamma_{xy}^2}{n_h^2-n_p^2}\right\}\alpha_E^2, \quad (18b)$$

whereas the electric-field dependence of the angle ψ_d is approximately linear: $\psi_d \propto E$ [$\tan(2\psi_d)\approx 2\psi_d = \gamma_{xy}\alpha_E/\Delta\epsilon \propto E$]. This effect is caused by the electrically induced distortions of the helical structure and bears some resemblance to the electro-optic Kerr effect. Following Refs. [15,16], it will be referred to as the orientational Kerr effect.

It should be emphasized that this effect differs from the well-known Kerr effect, which is a quadratic electro-optic effect related to the electrically induced birefringence in optically isotropic (and transparent) materials [35]. Similar to polymer stabilized blue phase liquid crystals [36,37], it is governed by the effective dielectric tensor of a nanostructured chiral smectic liquid crystal. This tensor is defined through averaging over the FLC orientational structure (see Appendix A).

III. EXPERIMENT

In this section we present the experimental results on the principal refractive indices and orientation of the in-plane optical axis measured as a function of the applied electric field in DHFLC cells.

A. Material and sample preparation

In our experiments we use the FLC mixture FLC-587 (from P. N. Lebedev Physical Institute of Russian Academy of Sciences) as the material for the DHFLC layer. The FLC-587 is an eutectic mixture of the three compounds whose chemical

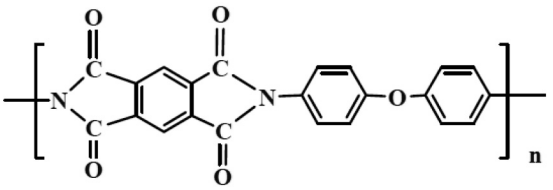

FIG. 2. Chemical structure of the compound forming the aligning layer.

structures are described in Ref. [15]. The phase transition sequence of this FLC during heating from the solid crystalline phase is Cr $\xrightarrow{+12\,^\circ\mathrm{C}}$ Sm-$C^\star$ $\xrightarrow{+110\,^\circ\mathrm{C}}$ Sm-$A^\star$ $\xrightarrow{+127\,^\circ\mathrm{C}}$ Is, while cooling from smectic-$C^\star$ phase crystallization occurs around $-10\,^\circ\mathrm{C}-15\,^\circ\mathrm{C}$. The spontaneous polarization P_s and the helix pitch P at room temperature (22 °C) are 150 nC/cm^2 and 150 nm, respectively.

The cell is sandwiched between two glass substrates covered by indium tin oxide (ITO) and aligning films with a thickness of 20 nm and the gap is fixed by spacers at $D = 50$ μm. The geometry of the cells is schematically depicted in Fig. 1(b).

High-quality planar alignment yielding a contrast ratio up to 200:1 is achieved using 4,4′-oxydianiline dianhydride (PMDA-ODA) as aligning layers. The chemical formula of this polyimide after imidization is shown in Fig. 2.

The PMDA-ODA dissolved in dimethyl-formamide (the concentration was about 0.2 wt. %) is spin coated onto the ITO surface. The polyimide film then is dried on the ITO substrate for 30–40 min at a temperature of 180 °C, and subsequent imidization is done at a temperature within the interval 275 °C−290 °C for about 1 h.

Following the method of Ref. [38], after cooling, the polyimide films are rubbed with a cotton shred to provide the aligning layers anisotropy. The FLC mixture is then injected into the cells in the isotropic phase by capillary action.

Our task is to obtain regular helix alignment in the cell with the helix axis parallel to the glass plates. For this purpose, the FLC cell is subjected to an additional electrical training with a square-wave function of maximum field amplitude ranging from 5 to 9 V/μm and the frequency in the range between 0.5 Hz and 2 kHz [39]. The obtained alignment is inspected by observing textures within the cell in a polarizing microscope.

B. Measurement of the azimuthal angle of the in-plane optical axis

In our experiments we use a low-power He-Ne laser ($\lambda = 632.8$ nm) as a light source. Initially, without applied voltage, the FLC cell is placed between the crossed polarizers and rotated so as to minimize the transmission of normally incident light. Then the cell is subjected to the time-varying voltage of the symmetric square-wave form with a frequency of 40 Hz and the amplitude ranges from zero to 100 V. Under the action of the applied electric field, the in-plane optical axis rotates about the normal to the substrates (the z axis) and its azimuthal angle ψ_d changes.

The angle ψ_d characterizing the electric-field-induced in-plane reorientation of the optical axis is measured by rotating the cell around the z axis and detecting the angle where the intensity of the transmitted light at positive voltages is minimal. The experimental results for this angle obtained at different values of the voltage amplitude are presented in Fig. 3.

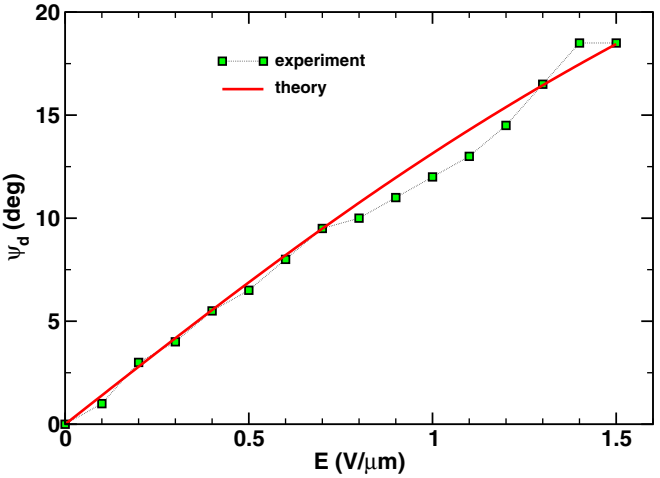

FIG. 3. (Color online) Azimuthal angle ψ_d of the major in-plane optical axis as a function of the electric field for the DHFLC cell of thickness $D = 50$ μm filled with the FLC mixture FLC-587 [15]. The experimental points are marked by squares. The solid line represents the theoretical curve computed from Eq. (17) with $P_s/\chi_E \approx 4.83$ V/μm. The following are the parameters of the mixture: $n_\perp \approx 1.52$ ($\epsilon_\perp \approx 2.3$) is the ordinary refractive index, $n_\parallel \approx 1.77$ ($\epsilon_\parallel \equiv \epsilon_1 \approx 3.13$) is the extraordinary refractive index, $\theta = 35.5^\circ$ is the tilt angle, and $r_2 = 1.05$ is the biaxiality ratio.

C. Measurement of the principal in-plane refractive indices

In order to perform measurements of the principal values of the in-plane refractive indices n_+ and n_- [see Eq. (12)], we use the well-known experimental method that is based on a Mach-Zehnder two-arm interferometer (it is detailed in many textbooks such as [40]). In this method, as can be seen in Fig. 4, a beam splitter divides a linearly polarized incident light passed through the input polarizer into two paths and the FLC cell is placed in the path of the sample beam. The sample and reference beams are then recombined and pass through the output polarizer so that the interfering beams after the polarizer are collected by a photodiode.

Given the amplitude of the voltage and the corresponding value of the principal axis azimuthal angle ψ_d, the polarizers are rotated so that the polarization vector of the incident light is either parallel or perpendicular to the optical axis. In both cases, measurements giving the electrically controlled part of the corresponding refractive index are performed during the half-period of positive applied voltage. The results are shown in Fig. 5.

D. Results

There are three optical characteristics of the DHFLC cell that we measure in our experiments: the azimuthal angle of the optical axis ψ_d and the electrically controlled parts of two principal refractive indices $\Delta n_\pm = n_\pm(E) - n_\pm(0)$. The experimental data for the electric-field dependence of the

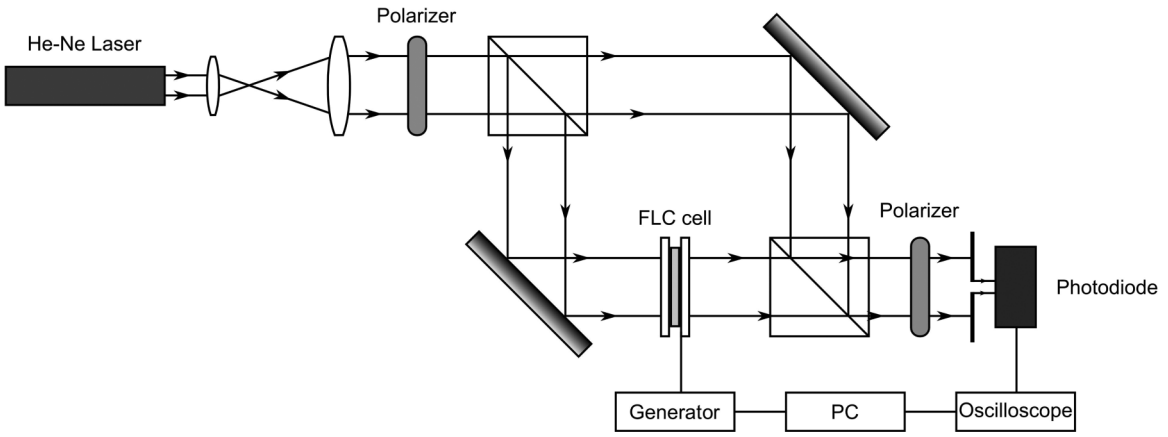

FIG. 4. Experimental setup for measurements of the electrically controlled parts of the in-plane refractive indices of the DHFLC cell.

principal axis angle and $\Delta n_{\pm}$ are presented in Figs. 3 and 5, respectively.

We can now use formulas for $n_{\pm}$ [see Eq. (12)] and ψ_d [see Eq. (17)] to fit the experimental data. For this purpose, we assume that the FLC mixture is characterized by the parameters $\epsilon_{\perp} \approx 2.3$ ($n_{\perp} \equiv n_o \approx 1.52$), $\epsilon_{\parallel} = 3.13$ ($n_{\parallel} \equiv n_e \approx 1.77$), and $\theta = 35.5^{\circ}$. Then the fitting gives the values of ratios $P_s/\chi_E \approx 4.83$ V/μm and $r_2 = \epsilon_2/\epsilon_{\perp} = 1.05$ that are regarded as the fitting parameters. The theoretical curves are shown in Figs. 3–5. Interestingly, the value of the biaxiality ratio differs from unity and thus the optical anisotropy of the mixture appears to be weakly biaxial.

Note that the fitted values of the zero-field refractive indices are $n_h \approx 1.67$ and $n_p \approx 1.57$. Figure 6 shows how the principal refractive indices $n_{\pm}$ and n_z change with the applied electric field. It is clear that electric-field-induced optical anisotropy is weakly biaxial with $n_z - n_- \ll n_+ - n_-$.

IV. LIGHT MODULATION IN DHFLC CELLS

In this section modulation of light in the DHFLC cells studied in the previous section will be of our primary concern. For both the transmissive and reflective modes, the DHFLC modulator is found to be affected by the presence of amplitude modulation. We study how this modulation influences the transformation characteristics of a DHFLC spatial light modulator operating as an axicon producing a ring-shaped far-field distribution of light.

A. Amplitudes and phases

Typically, in experiments dealing with the electro-optic response of DHFLC cells, the transmittance of normally incident light passing through crossed polarizers is measured as a function of the applied electric field. In the case of normal incidence, the transmission and reflection matrices can be easily obtained from the results of Refs. [21,41,42] in the limit of the wave vectors with vanishing tangential component $k_p = 0$. For our purposes, we need to write down the resultant expression for the transmission matrix

$$\mathbf{T}(\psi_d) = \frac{t_+ + t_-}{2}\mathbf{I}_2 + \frac{t_+ - t_-}{2}\mathbf{Rt}(2\psi_d)\sigma_3, \qquad (19)$$

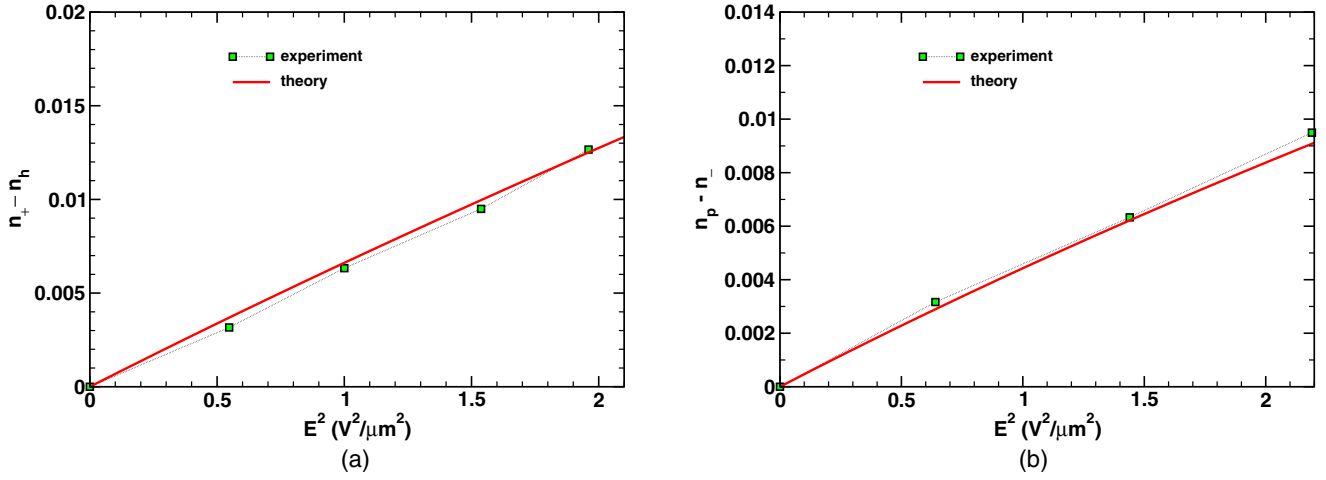

FIG. 5. (Color online) Electrically controlled differences of the principal in-plane refractive indices (a) Δn_+ [$= n_+(E) - n_+(0)$] and (b) $-\Delta n_-$ [$= n_-(0) - n_-(E)$] as a function of the square of the applied electric field. Solid lines represent the theoretical curves computed from Eq. (12) using the parameters listed in the caption of Fig. 3.

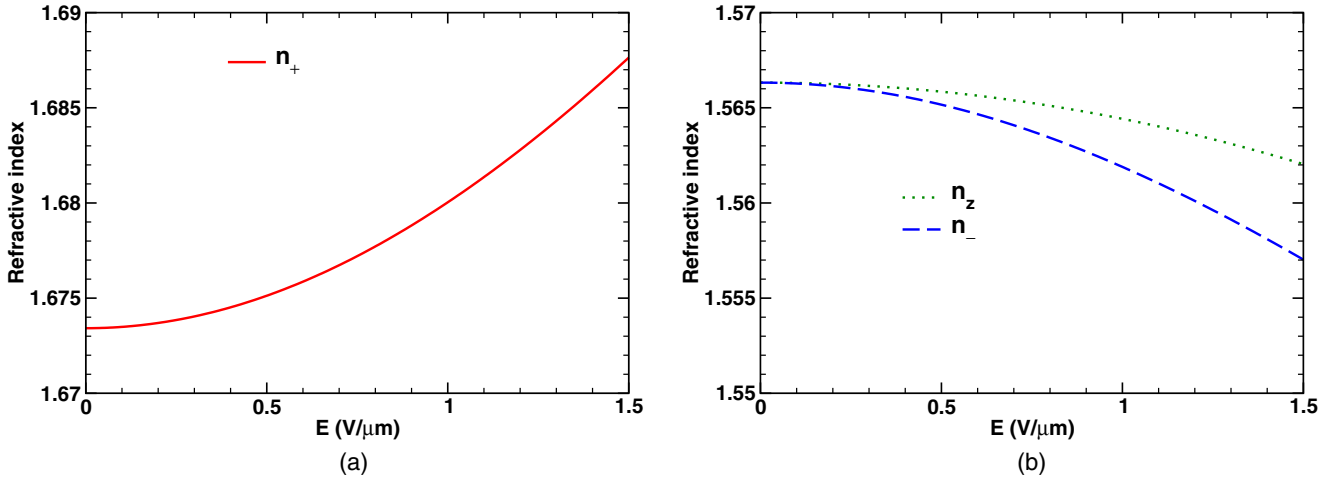

FIG. 6. (Color online) Electric-field dependence of principal refractive indices (a) n_+ and (b) $n_{z,-}$.

$$t_\pm = \frac{1-\rho_\pm^2}{1-\rho_\pm^2\exp(2in_\pm h)}\exp(in_\pm h), \tag{20}$$

$$\rho_\pm = \frac{n_\pm/\mu - n_m/\mu_m}{n_\pm/\mu + n_m/\mu_m}, \tag{21}$$

where

$$\mathbf{I}_2 = \begin{pmatrix} 1 & 0 \\ 0 & 1 \end{pmatrix}, \quad \boldsymbol{\sigma}_3 = \begin{pmatrix} 1 & 0 \\ 0 & -1 \end{pmatrix}, \tag{22a}$$

$$\mathbf{Rt}(2\psi_d) \equiv \begin{pmatrix} \cos 2\psi_d & -\sin 2\psi_d \\ \sin 2\psi_d & \cos 2\psi_d \end{pmatrix}, \tag{22b}$$

and $h = k_{vac}D$ is the thickness parameter. Equation (19) defines the transmission matrix linking the vector amplitudes of incident and transmitted waves $\mathbf{E}_0$ and $\mathbf{E}_{transm}$ through the standard input-output relation

$$\mathbf{E}_{transm} = \mathbf{T}(\psi_d)\mathbf{E}_0, \quad \mathbf{E}_{transm} = \begin{pmatrix} E_x^{(transm)} \\ E_y^{(transm)} \end{pmatrix}. \tag{23}$$

When the incident wave is linearly polarized along the x axis (the helix axis) with

$$\mathbf{E}_0 = \begin{pmatrix} E_0 \\ 0 \end{pmatrix}, \tag{24}$$

the components of the transmitted wave can be written in the form

$$\begin{aligned} E_x^{(transm)}/E_0 &= A_x\exp(i\phi_x) = t_+ - (t_+ - t_-)\sin^2\psi_d, \\ E_y^{(transm)}/E_0 &= A_y\exp(i\phi_y) = \frac{t_+ - t_-}{2}\sin(2\psi_d), \end{aligned} \tag{25}$$

where $A_{x,y}$ and $\phi_{x,y}$ are the normalized amplitude and phase of the corresponding complex amplitude component, respectively. Then the transmittance coefficient describing the intensity of the light passing through crossed polarizers is given by

$$|A_y|^2 = \frac{|t_+ - t_-|^2}{4}\sin^2(2\psi_d). \tag{26}$$

Note that, under certain conditions such as $|\rho_\pm| \ll 1$, both the transmission coefficients (20) and the transmittance (26) can be approximated by simpler formulas

$$t_\pm \approx \exp(i\Phi_\pm), \quad \Phi_\pm = n_\pm h, \tag{27a}$$

$$\frac{t_+ - t_-}{2} \approx \sin(\Delta\Phi/2)\exp[i(\Phi_+ + \Phi_- + \pi)/2], \tag{27b}$$

$$|A_y|^2 \approx \sin^2(\Delta\Phi/2)\sin^2(2\psi_d), \tag{27c}$$

where $\Delta\Phi = \Phi_+ - \Phi_-$ is the difference in optical path of the ordinary and extraordinary waves known as the phase retardation.

The complex-valued components of the transmitted plane wave are thus characterized by the amplitudes and phases $A_{x,y}$ and $\phi_{x,y}$ given in Eq. (25). These can now be computed as a function of the applied electric field by using our experimental data combined with the results of fitting presented in Sec. III D. Referring to Fig. 7, rotation of the optical axis combined with electric-field-induced change in the phase retardation produces variations of the amplitudes A_x and A_y with the electric field.

For the component parallel to the helix axis E_x, the amplitude modulation, however, has a negligibly small effect on the electric-field dependence of the phase ϕ_x. It turns out that, despite amplitude modulation, this phase is close to Φ_+: $\phi_x \approx \Phi_+$.

From Eq. (27c) it might be concluded that the phase of the component perpendicular to the helix axis ϕ_y is given by $(\Phi_+ + \Phi_- + \pi)/2$. It should be noted that, in the approximation described by Eq. (27a), when the factor $\sin(\Delta\Phi/2)$ changes its sign at the points where the amplitude A_y (and T_{xy}) is zero, the phase should experience jumplike behavior with $\Delta\phi_x = \pm\pi$. These jumps are not shown in Fig. 7 as, in real experiments, the amplitude A_y never reaches zero due to scattering effects.

We have also computed the amplitudes and phases of the reflected wave for the DHFLC cell operating in the reflective mode with the mirror placed at the exit face of the cell. It can be shown that, for the case of normal incidence, the reflection matrix can be written as (details are relegated to

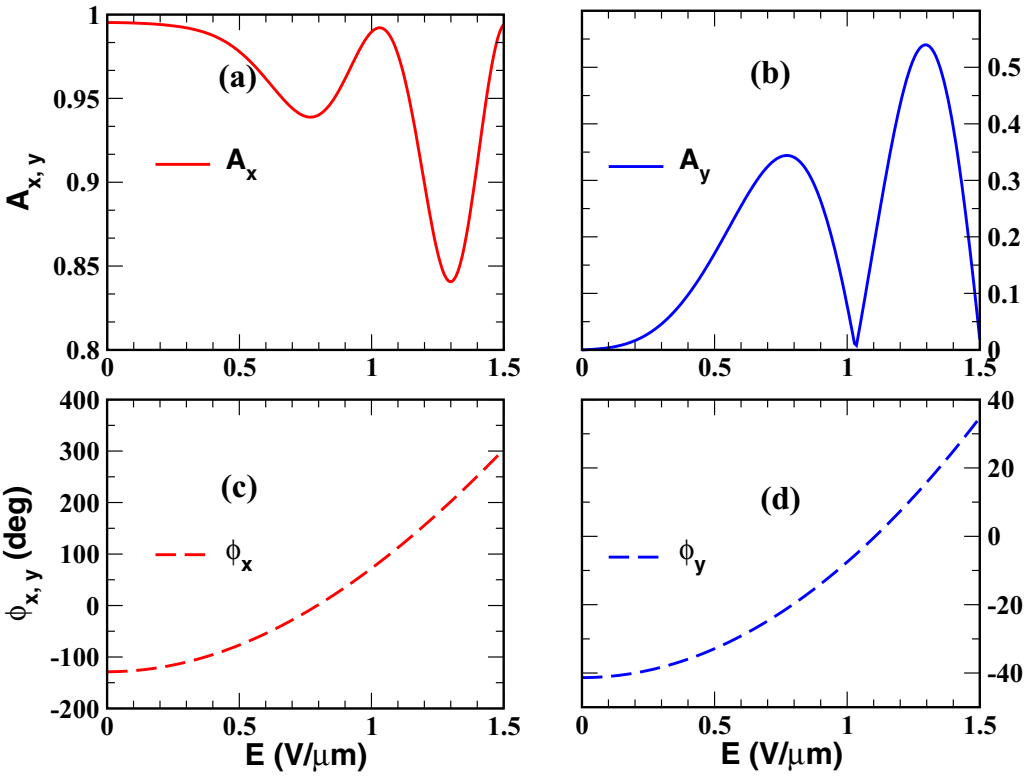

FIG. 7. (Color online) Amplitudes (a) A_x and (b) A_y and phases (c) ϕ_x and (d) ϕ_y for the components of the transmitted light vector amplitude $\mathbf{E}_{\text{transm}}/E_0$ computed as a function of the applied electric field in the transmissive mode.

Appendix B)

$$\mathbf{R}(\psi_d) = \frac{r_+ + r_-}{2}\boldsymbol{\sigma}_3 + \frac{r_+ - r_-}{2}\mathbf{R}\mathbf{t}(-2\psi_d), \tag{28}$$

$$r_\pm = \frac{\rho_\pm + \tilde{\rho}_\pm \exp(2i\Phi_\pm)}{1 + \rho_\pm\tilde{\rho}_\pm \exp(2i\Phi_\pm)}, \quad \tilde{\rho}_\pm = \frac{R_r - \rho_\pm}{1 - R_r\rho_\pm}, \tag{29}$$

where R_r is the reflection coefficient of the mirror given by

$$R_r = \rho_r \frac{1 - \exp(2in_r h_r)}{1 - \rho_r^2 \exp(2in_r h_r)}, \quad \rho_r = \frac{n_r/\mu_r - n_\text{m}/\mu_\text{m}}{n_r/\mu_r + n_\text{m}/\mu_\text{m}}. \tag{30}$$

Here n_r (μ_r) and $h_r = k_\text{vac} D_r$ (D_r) are the mirror refractive index (magnetic permittivity) and the thickness parameter (thickness) of the mirror, respectively.

In the reflective mode, for the incident wave (24), the input-output relation

$$\mathbf{E}_\text{refl} = \mathbf{R}(\psi_d)\mathbf{E}_0, \quad \mathbf{E}_\text{refl} = \begin{pmatrix} E_x^{(\text{refl})} \\ E_y^{(\text{refl})} \end{pmatrix} \tag{31}$$

gives the components of the reflected wave

$$\begin{aligned} E_x^{(\text{refl})}/E_0 &= A_x \exp(i\phi_x) = r_+ - (r_+ - r_-)\sin^2\psi_d, \\ E_y^{(\text{refl})}/E_0 &= A_y \exp(i\phi_y) = -\frac{r_+ - r_-}{2}\sin(2\psi_d). \end{aligned} \tag{32}$$

The curves depicted in Fig. 8 as solid lines are computed for the silver mirror of the thickness $D_r = 0.15$ μm, which is characterized by the complex-valued refractive index [43] $n_r \approx 0.16 + 3.8i$ at the wavelength $\lambda = 633$ nm. The magnitude and the phase of the reflection coefficient (30) $R_r = |R_r|\exp(i\phi_r)$ then can be estimated at about $|R_r| \approx 0.97$ and $\phi_r \approx 43^\circ$.

Alternatively, the reflective mode can be described in the double-layer approximation, which is based on the assumption of perfect reflection. It uses the transmission matrix (19) where the thickness of the cell is doubled and D is replaced by $2D$. The results computed in this approximation are shown in Fig. 8 as dotted lines. Interestingly, for the amplitude modulation of the component A_y, the exact and approximated results are in excellent agreement. By contrast, the curves for the magnitude of the component A_x [see Fig. 8(a)] noticeably differ from each other. It comes as no surprise that the double-layer approximation overestimates $|A_x|$.

Similar to the transmissive mode, the results for the phases ϕ_x and ϕ_y can be easily understood in the limiting case where $|\rho_\pm|$ are small and the reflection coefficients $r_\pm$ defined in Eq. (29) are close to $R_r \exp(2i\Phi_\pm)$. From Eq. (32) it can be inferred that $\phi_x \approx 2\Phi_+ + \phi_r$ and $\phi_y \approx \Phi_+ + \Phi_- + \phi_r + 3\pi/2$, whereas the double-layer approximation gives the relations $\phi_x \approx 2\Phi_+$ and $\phi_y \approx \Phi_+ + \Phi_- + \pi/2$. The curves plotted in Figs. 8(c) and 8(d) clearly show the phase shift introduced by the mirror and the minus sign on the right-hand side of Eq. (32) for the component A_y. It can also be seen that phase modulation is about two times larger compared to the case of the transmissive mode. So the electric field required to reach 2π modulation is reduced by a factor of about 1.4.

B. Axicon

The liquid crystal spatial light modulators are extensively used for formation of light wave fields with a specified

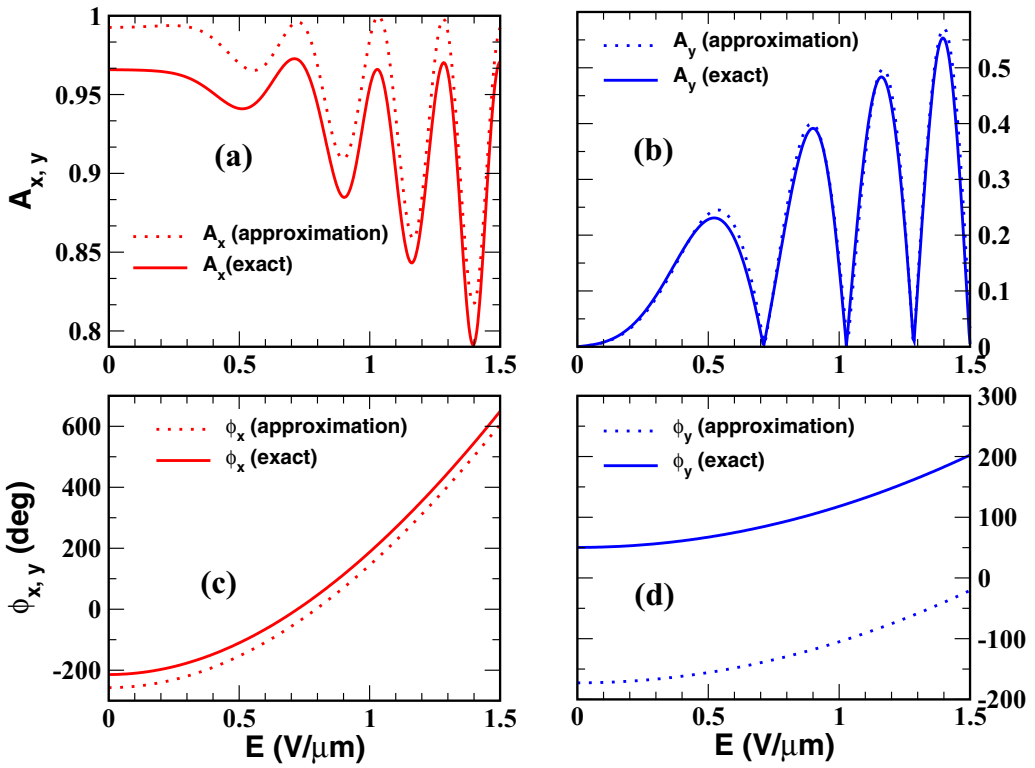

FIG. 8. (Color online) Amplitudes (a) A_x and (b) A_y and phases (c) ϕ_x and (d) ϕ_y for the components of the reflected light vector amplitude $\mathbf{E}_{\text{refl}}/E_0$ computed as a function of the applied electric field in the reflective mode. Dotted lines represent the curves computed from Eq. (25) with the double-layer thickness (D is replaced by $2D$). Solid curves are evaluated using the reflection matrix (28) and Eq. (32).

spatial distribution of intensity. The above discussed effects of amplitude modulation may affect the quality of the resulting light field. In order to estimate how these effects influence a reflective DHFLC modulator, we have modeled the DHFLC SLM as a 2D array of 256×256 pixels each of an area of 200×200 μm^2. It should be noted that in our model the electric field is assumed to be uniform. In our case, the pixel size to cell thickness ratio is large enough for this assumption to be justified.

In our calculations we assume that the incident wave is linearly polarized along the helix axis (x axis) and the phase distribution in the plane of the modulator is equivalent to the phase profile of an axicon given by

$$\phi_x(x_0,y_0) = -\Phi_{\text{axicon}}\frac{\rho_0}{R}, \quad \rho_0 = \sqrt{x_0^2+y_0^2}, \tag{33}$$

where $k = 2\pi/\lambda$ is the wave number, f is the focal length, R is the axicon radius, and Φ_{axicon} is the phase modulation depth of the axicon. The x component of the light field in the focal plane of lens can be computed from the Fresnel-Kirchhoff diffraction formula taken in the far-field (Fraunhofer) approximation (see, e.g., Ref. [44])

$$E_x(x,y) = \frac{\exp\left[ikf + \frac{ik(x^2+y^2)}{2f}\right]}{i\lambda f}\int_{-\infty}^{\infty}\int_{-\infty}^{\infty} A_x(x_0,y_0) \times \exp\left[i\phi_x(x_0,y_0) - \frac{ik}{f}\{xx_0+yy_0\}\right]dx_0dy_0. \tag{34}$$

The amplitude and phase distributions $A_x(x_0,y_0)$ and $\phi_x(x_0,y_0)$ that enter the integrand on the right-hand side of Eq. (34) are approximated as follows: (a) We recast the phase profile of an axicon characterized by the specified depth of modulation into the steplike form with the step height equal to 2π; (b) the spatial phase distribution is then discretized along the coordinates x and y with $\Delta x = \Delta y = 200$ μm so that each pixel is characterized by the constant phase equal to the value of ϕ_x in its center; (c) for each value of the phase ϕ_x, we compute the corresponding value of the amplitude A_x and derive the discretized distribution of the amplitude. The final step involves using the standard fast Fourier transform technique [45] to evaluate the integral on the right-hand side of Eq. (34).

Figure 9 shows the phase and amplitude distributions that were computed for the modulation depth Φ_{axicon} equal to 16π. The intensity distribution in the focal plane and the corresponding x dependence of the intensity are presented in Figs. 10 and 11, respectively. In Fig. 11 the case of the DHFLC axicon (dashed line) [see Fig. 10(a)] is compared with the curve (solid line) computed for an ideal axicon without amplitude modulation [see Fig. 10(b)]. The latter implies that the amplitude $A_x(x_0,y_0)$ is assumed to be constant. For the curves depicted in Fig. 11, the loss of power caused by amplitude modulation can be estimated to be below 5%.

Note that the results shown in Figs. 9–11 are computed at a DHFLC cell thickness taken to be about 50 μ m. We have also found that when the thickness of the DHFLC cells is halved, reducing the thickness results in an increase of the power loss that can be estimated at about 11%.

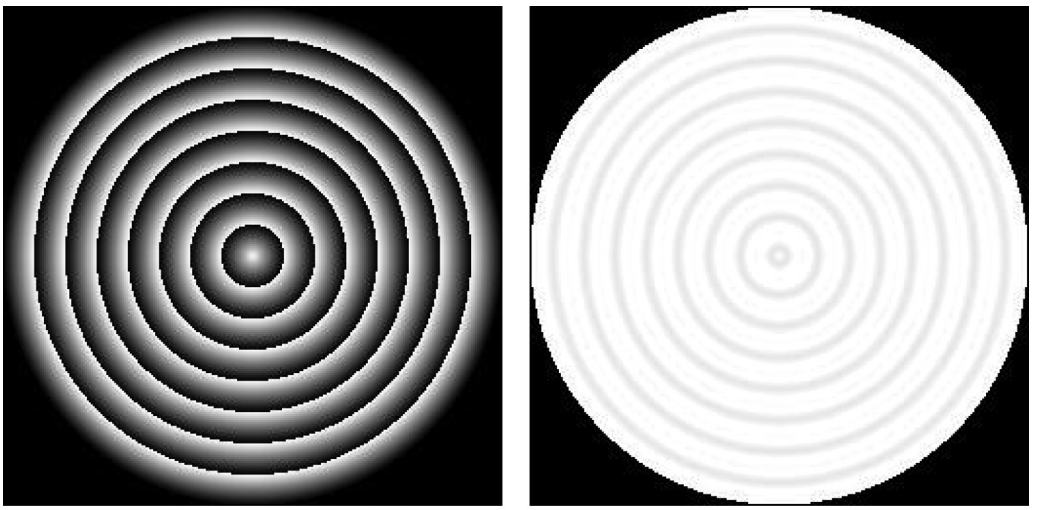

(a) (b)

FIG. 9. Profiles of (a) phase ϕ_x and (b) amplitude A_x in the transverse plane of the DHFLC spatial light modulator. Grayscale with 256 levels of gray encodes the values of ϕ_x and A_x ranging from zero (black) to 2π and unity (white), respectively.

V. DISCUSSION AND CONCLUSION

In this paper we have studied optical properties of the planar aligned DHFLC cells (geometry shown in Fig. 1) that govern modulation of light in such cells. In our experiments we have combined the experimental data for the electric-field dependence of in-plane optical axis orientation characterized by the azimuthal angle ψ_d (see Fig. 3) with the experimental technique based on the Mach-Zehnder interferometer to measure the principal refractive indices as a function of the electric field (see Fig. 5).

A general expression for the effective optical tensor of a DHFLC cell derived in Ref. [21] [see Eq. (6)] was used to fit the experimental curves. The obtained parameters of the FLC mixture FLC-587 show that this material is a weakly biaxial FLC. Similarly, the resulting electric-field dependence of the principal effective refractive indices of the DHFLC cell plotted in Fig. 6 clearly indicate electric-field-induced optical biaxiality of the effective dielectric tensor (6). Note that optical biaxiality of the smectic-C^* phase was previously reported in Refs. [46–48].

Note that our theoretical analysis assumes an ideal (undistorted) bookshelf structure of smectics layers in DHFLC cells [see Fig. 1(b)]. This assumption is justified by the fact that, in contrast to the case of SSFLCs, in DHFLC cells, chevron structures and related zigzag defects [49] have never been observed and reported in the literature, whereas the photos of perfect chevron-free textures formed in DHFLC cells can be found, e.g., in Refs. [15,39,50].

All the DHFLCs that have been developed by our group and used in our experiments are 100% composed of molecules with rigid molecular cores (the chemical structure of DHFLC-587

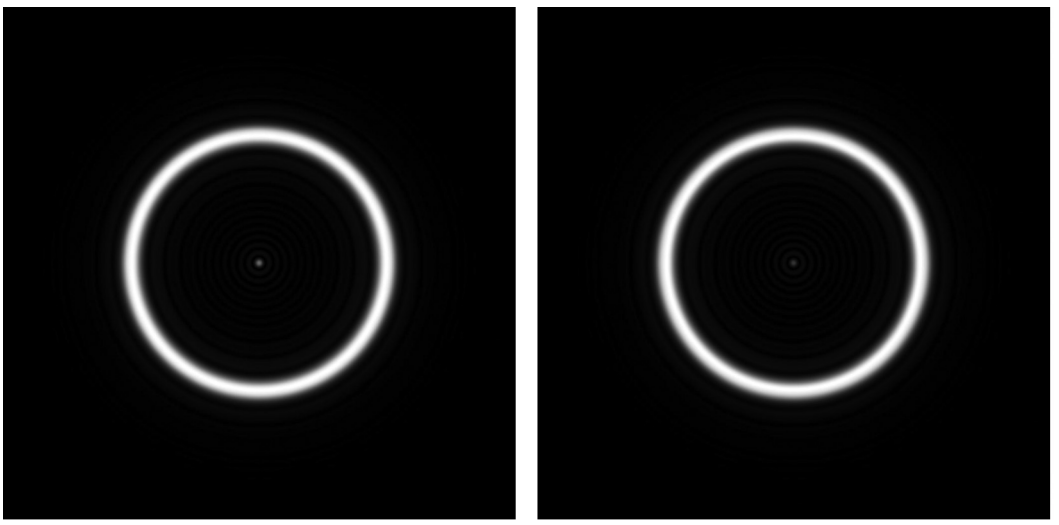

(a) (b)

FIG. 10. Grayscale representation of the intensity distribution in the focal plane of (a) the DHFLC and (b) ideal (no amplitude modulation) axicons operating in the reflective mode. The cell thickness is about 50 μm.

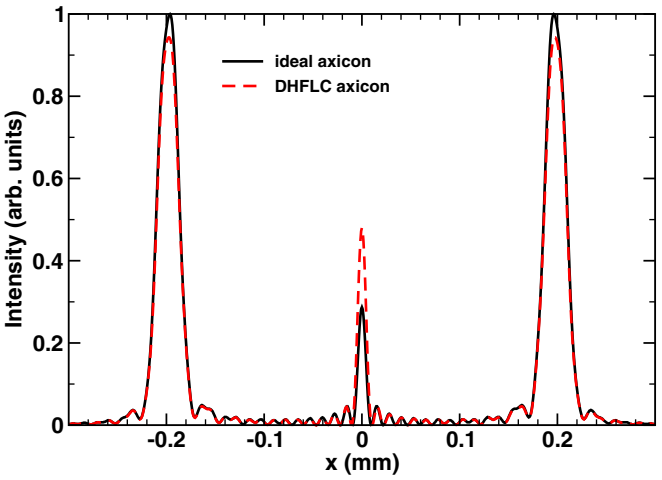

FIG. 11. (Color online) Intensity in the focal plane as a function of x for the DHFLC and ideal operating in the reflective mode. The solid line represents the distribution computed for the case of an ideal axicon without amplitude modulation. The cell thickness is about 50 μm.

is described in Ref. [15]). So, in our case, the well-known condition for the formation of chevron-free structures [51,52], which requires the concentration of molecules with rigid molecular cores in an FLC mixture to exceed a certain limiting value, is satisfied. This can be one of the reasons why the chevron structures appear to be suppressed in the DHFLC cells. Interestingly, similar molecular structures have recently been found to be favorable for the de Vries type of FLC [53] and thus the DHFLCs under consideration could be of the de Vries type. Nevertheless, it should be stressed that additional research is needed to unambiguously identify the nature of the observed chevron-free structure of smectic layers in the DHFLC cells. Such a study is beyond the scope of this paper.

We have analyzed modulation of light in the DHFLC cell under consideration by computing the amplitudes and phases of the components of the light wave transmitted through (reflected from) the cell in the transmissive (reflective) mode described using the transfer matrix approach [21]. It has been found that, in addition to phase modulation, electric-field-induced birefringence and rotation of the in-plane optical axes generally result in the effects of amplitude modulation. Additionally, we have calculated the far-field intensity distribution formed by the DHFLC spatial light modulator operating as an axicon. From a comparison between the results obtained for the ideal (no amplitude modulation) axicon and the DHFLC modulator, it can be concluded that the characteristics of the DHFLC axicon are very close to the ones of the ideal axicon. In particular, for a cell thickness of about 50 μm the power loss due to amplitude modulation is estimated at about 5%, whereas it increases up to 11% for the halved thickness. For many applications, such values of power loss can be regarded as acceptable. Note that, according to Ref. [54], the vortex light-wave fields shaped in the form of certain curves, which are of importance for efficient laser micromanipulation, can be generated using the 2D array made up of at least 128 $\times$ 128 amplitude-phase diffractive elements.

In addition, the typical response time of the DHFLC modulator based on FLC-587 is known to be around 100 μs at a phase shift equal to π [17]. So it might be concluded that all essential prerequisites are in place for elaboration of the DHFLC spatial light modulator operating almost as the ideal axicon at a phase modulation frequency of about 1 kHz.

ACKNOWLEDGMENTS

This work was supported by the RFBR Project No. 13-02-00598_a. A.D.K. acknowledges partial financial support from the Government of the Russian Federation (Grant No. 074-U01), from the Ministry of Education and Science of the Russian Federation (Grant No. GOSZADANIE 2014/190, Project No. 14.Z50.31.0031, and ZADANIE Grant No. 1.754.2014/K), through a grant from the Russian Foundation for Basic Research, and through a grant from the President of Russia (Grant No. MK-2736.2015.2).

APPENDIX A: EFFECTIVE DIELECTRIC TENSOR

According to Ref. [20], the effective dielectric tensor

$$\boldsymbol{\varepsilon}_{\text{eff}} = \begin{pmatrix} \epsilon_{xx}^{(\text{eff})} & \epsilon_{xy}^{(\text{eff})} & \epsilon_{xz}^{(\text{eff})} \\ \epsilon_{yx}^{(\text{eff})} & \epsilon_{yy}^{(\text{eff})} & \epsilon_{yz}^{(\text{eff})} \\ \epsilon_{zx}^{(\text{eff})} & \epsilon_{zy}^{(\text{eff})} & \epsilon_{zz}^{(\text{eff})} \end{pmatrix} \tag{A1}$$

can be expressed in terms of the averages

$$\eta_{zz} = \langle \epsilon_{zz}^{-1} \rangle = \epsilon_0^{-1} \langle [1 + u_1 d_z^2 + u_2 p_z^2]^{-1} \rangle, \tag{A2}$$

$$\beta_{z\alpha} = \langle \epsilon_{z\alpha}/\epsilon_{zz} \rangle = \left\langle \frac{u_1 d_z d_\alpha + u_2 p_z p_\alpha}{1 + u_1 d_z^2 + u_2 p_z^2} \right\rangle, \tag{A3}$$

where $\langle \cdots \rangle \equiv \langle \cdots \rangle_\phi = (2\pi)^{-1} \int_0^{2\pi} \cdots d\phi$ and $\alpha \in \{x, y\}$, as follows:

$$\begin{aligned} \epsilon_{zz}^{(\text{eff})} &= 1/\eta_{zz}, \quad \epsilon_{z\alpha}^{(\text{eff})} = \beta_{z\alpha}/\eta_{zz}, \\ \epsilon_{\alpha\beta}^{(\text{eff})} &= \langle \epsilon_{\alpha\beta}^{(P)} \rangle + \beta_{z\alpha}\beta_{z\beta}/\eta_{zz}, \end{aligned} \tag{A4}$$

where $\langle \epsilon_{\alpha\beta}^{(P)} \rangle$ are the components of the averaged tensor $\langle \boldsymbol{\varepsilon}_P \rangle$,

$$\begin{aligned} \langle \epsilon_{\alpha\beta}^{(P)} \rangle &= \left\langle \epsilon_{\alpha\beta} - \frac{\epsilon_{\alpha z}\epsilon_{z\beta}}{\epsilon_{zz}} \right\rangle \\ &= \epsilon_0 \left\langle \delta_{\alpha\beta} + \frac{u_1 d_\alpha d_\beta + u_2 p_\alpha p_\beta + u_1 u_2 q_\alpha q_\beta}{1 + u_1 d_z^2 + u_2 p_z^2} \right\rangle, \end{aligned} \tag{A5}$$

$$q_\alpha = p_z d_\alpha - d_z p_\alpha, \quad \alpha, \beta \in \{x, y\}, \tag{A6}$$

describing effective in-plane anisotropy that governs propagation of normally incident plane waves. The general formulas (A2)–(A6) give the zeroth-order approximation for homogeneous models describing the optical properties of short-pitch DHFLCs [15,20].

APPENDIX B: DERIVATION OF THE REFLECTION MATRIX

In this Appendix our task is to derive the reflection matrix (28) for the plane wave normally incident on the DHFLC cell whose exit face is covered with a thin reflecting layer (mirror).

For this purpose we use the transfer matrix approach in the form presented in Refs. [21,42,55]. We begin with the 4×4 transfer matrix

$$\mathbf{W} = \begin{pmatrix} \mathbf{W}_{11} & \mathbf{W}_{12} \\ \mathbf{W}_{21} & \mathbf{W}_{22} \end{pmatrix} = \mathbf{W}_{\mathrm{FLC}}\mathbf{W}_r, \tag{B1}$$

where $\mathbf{W}_{ij}$ are 2×2 block matrices, expressed as a product of the transfer matrices of the FLC cell $\mathbf{W}_{\mathrm{FLC}}$ and the mirror $\mathbf{W}_r$. Given the transfer matrix (B1), the transmission and reflection matrices $\mathbf{T}$ and $\mathbf{R}$, respectively, can generally be computed from the formulas (see, e.g., Ref. [21])

$$\mathbf{T} = \mathbf{W}_{11}^{-1}, \quad \mathbf{R} = \mathbf{W}_{21}\mathbf{W}_{11}^{-1} \tag{B2}$$

that relate $\mathbf{T}$ and $\mathbf{R}$ with the block matrices $\mathbf{W}_{11}$ and $\mathbf{W}_{21}$.

Applying Eq. (B2) to the case of light normally impinging upon the FLC layer characterized by the dielectric tensor (10) gives the transmission matrix

$$\begin{aligned} \mathbf{T}_{\mathrm{FLC}} &= \left[\mathbf{W}_{11}^{(\mathrm{FLC})}\right]^{-1} \\ &= \mathbf{Rt}(\psi_{\mathrm{d}}) \begin{pmatrix} t_{+}^{(\mathrm{FLC})} & 0 \\ 0 & t_{-}^{(\mathrm{FLC})} \end{pmatrix} \mathbf{Rt}(-\psi_{\mathrm{d}}), \end{aligned} \tag{B3}$$

$$t_{\pm}^{(\mathrm{FLC})} = \frac{1-\rho_{\pm}^2}{1-\rho_{\pm}^2 \exp(2in_{\pm}h)} \exp(in_{\pm}h), \tag{B4}$$

$$\rho_{\pm} = \frac{n_{\pm}/\mu - n_{\mathrm{m}}/\mu_{\mathrm{m}}}{n_{\pm}/\mu + n_{\mathrm{m}}/\mu_{\mathrm{m}}}, \tag{B5}$$

where $\mathbf{Rt}(\psi_{\mathrm{d}})$ is the rotation matrix [see Eq. (22b)], which is identical to the matrix given in Eq. (19). The corresponding result for the reflection matrix reads

$$\begin{aligned} \mathbf{R}_{\mathrm{FLC}} &= \mathbf{W}_{21}^{(\mathrm{FLC})}\left[\mathbf{W}_{11}^{(\mathrm{FLC})}\right]^{-1} \\ &= \boldsymbol{\sigma}_3 \mathbf{Rt}(\psi_{\mathrm{d}}) \begin{pmatrix} r_{+}^{(\mathrm{FLC})} & 0 \\ 0 & r_{-}^{(\mathrm{FLC})} \end{pmatrix} \mathbf{Rt}(-\psi_{\mathrm{d}}), \end{aligned} \tag{B6}$$

$$r_{\pm}^{(\mathrm{FLC})} = \rho_{\pm} \frac{1-\exp(2in_{\pm}h)}{1-\rho_{\pm}^2 \exp(2in_{\pm}h)}. \tag{B7}$$

For the reflecting layer, the results

$$\mathbf{T}_r = \left[\mathbf{W}_{11}^{(r)}\right]^{-1} = T_r \mathbf{I}_2, \tag{B8a}$$

$$T_r = \frac{1-\rho_r^2}{1-\rho_r^2 \exp(2in_r h_r)} \exp(in_r h_r), \tag{B8b}$$

$$\mathbf{R}_r = \mathbf{W}_{21}^{(r)}\left[\mathbf{W}_{11}^{(r)}\right]^{-1} = R_r \boldsymbol{\sigma}_3, \tag{B8c}$$

$$R_r = \rho_r \frac{1-\exp(2in_r h_r)}{1-\rho_r^2 \exp(2in_r h_r)}, \quad \rho_r = \frac{n_r/\mu_r - n_{\mathrm{m}}/\mu_{\mathrm{m}}}{n_r/\mu_r + n_{\mathrm{m}}/\mu_{\mathrm{m}}} \tag{B8d}$$

can be obtained from the above formulas for the FLC layer by replacing $\{n_+, n_-, h = k_{\mathrm{vac}}D\}$ with $\{n_r, n_r, h_r = k_{\mathrm{vac}}D_r\}$.

For a nonabsorbing FLC material, the unitarity relations imply the symmetry conditions [21]

$$\left[\mathbf{W}_{ii}^{(\mathrm{FLC})}\right]^T = \mathbf{W}_{ii}^{(\mathrm{FLC})}, \quad \left[\mathbf{W}_{21}^{(\mathrm{FLC})}\right]^T = -\mathbf{W}_{12}^{(\mathrm{FLC})}, \tag{B9}$$

$$\left[\mathbf{W}_{11}^{(\mathrm{FLC})}\right]^{\dagger} = \boldsymbol{\sigma}_3 \mathbf{W}_{22}^{(\mathrm{FLC})} \boldsymbol{\sigma}_3, \tag{B10}$$

$$\left[\mathbf{W}_{21}^{(\mathrm{FLC})}\right]^{\dagger} = -\boldsymbol{\sigma}_3 \mathbf{W}_{21}^{(\mathrm{FLC})} \boldsymbol{\sigma}_3, \tag{B11}$$

where a dagger and the superscript T denote Hermitian conjugation and matrix transposition, respectively. The conditions (B9) can now be used to express the block matrix $\mathbf{W}_{11}$ in terms of the transmission and reflection matrices as

$$\begin{aligned} \mathbf{W}_{11} &= \mathbf{W}_{11}^{(\mathrm{FLC})}\mathbf{W}_{11}^{(r)} + \mathbf{W}_{12}^{(\mathrm{FLC})}\mathbf{W}_{21}^{(r)} \\ &= \left[\mathbf{W}_{11}^{(\mathrm{FLC})} + \mathbf{W}_{12}^{(\mathrm{FLC})}\mathbf{R}_r\right]\mathbf{T}_r^{-1} \\ &= \mathbf{T}_{\mathrm{FLC}}^{-1}\left[\mathbf{I}_2 - \mathbf{R}_{\mathrm{FLC}}^T\mathbf{R}_r\right]\mathbf{T}_r^{-1}. \end{aligned} \tag{B12}$$

Equation (B12), combined with the relation (B2), immediately gives the transmission matrix in the general form

$$\mathbf{T} = \mathbf{T}_r\left[\mathbf{I}_2 - \mathbf{R}_{\mathrm{FLC}}^T\mathbf{R}_r\right]^{-1}\mathbf{T}_{\mathrm{FLC}}. \tag{B13}$$

Similarly, using the symmetry relations (B10) and (B11), we can obtain the following result for the block matrix $\mathbf{W}_{21}$:

$$\begin{aligned} \mathbf{W}_{21} &= \mathbf{W}_{21}^{(\mathrm{FLC})}\mathbf{W}_{11}^{(r)} + \mathbf{W}_{22}^{(\mathrm{FLC})}\mathbf{W}_{21}^{(r)} \\ &= \left[\mathbf{W}_{21}^{(\mathrm{FLC})} + \mathbf{W}_{22}^{(\mathrm{FLC})}\mathbf{R}_r\right]\mathbf{T}_r^{-1} \\ &= \boldsymbol{\sigma}_3[\mathbf{T}_{\mathrm{FLC}}^{\dagger}]^{-1}\{\boldsymbol{\sigma}_3\mathbf{R}_r - [\boldsymbol{\sigma}_3\mathbf{R}_{\mathrm{FLC}}]^{\dagger}\}\mathbf{T}_r^{-1}. \end{aligned} \tag{B14}$$

Substituting formulas (B12) and (B14) into Eq. (B2) gives the resulting expression for the reflection matrix in the following form:

$$\begin{aligned} \mathbf{R} = \boldsymbol{\sigma}_3[\mathbf{T}_{\mathrm{FLC}}^{\dagger}]^{-1}\{\boldsymbol{\sigma}_3\mathbf{R}_r - [\boldsymbol{\sigma}_3\mathbf{R}_{\mathrm{FLC}}]^{\dagger}\} \\ \times \left[\mathbf{I}_2 - \mathbf{R}_{\mathrm{FLC}}^T\mathbf{R}_r\right]^{-1}\mathbf{T}_{\mathrm{FLC}}. \end{aligned} \tag{B15}$$

Formulas (B13) and (B15) are quite general. In particular, they can be applied to any nonabsorbing uniformly anisotropic layer represented by the FLC material. For the case of normal incidence, from Eqs. (B3)–(B8) it follows that, similar to the matrices $\mathbf{T}_{\mathrm{FLC}}(\psi_d)$ and $\mathbf{R}_{\mathrm{FLC}}(\psi_d)$, the matrices $\mathbf{T}(\psi_d)$ and $\mathbf{R}(\psi_d)$ can be recast into the following factorized form:

$$\mathbf{T}(\psi_d) = \mathbf{Rt}(\psi_d)\mathbf{T}(0)\mathbf{Rt}(-\psi_d), \tag{B16a}$$

$$\mathbf{R}(\psi_d) = \mathbf{Rt}(-\psi_d)\mathbf{R}(0)\mathbf{Rt}(-\psi_d). \tag{B16b}$$

The matrices $\mathbf{T}(0)$ and $\mathbf{R}(0)$ are diagonal and can be easily computed. After algebraic manipulations, it is not difficult to derive the analytical expression for the transmission matrix given in Eqs. (28)–(30).

[1] T. D. Wilkinson, Y. Petillot, R. J. Mears, and J. L. de Bougrenet de la Tocnaye, Scale-invariant optical correlators using ferroelectric liquid-crystal spatial light modulators, Appl. Opt. **34**, 1885 (1995).

[2] S. Kotova, M. Kvashnin, M. Rakhmatulin, O. Zayakin, I. Guralnik, N. Klimov, P. Clark, G. Love, A. Naumov, C. Saunter, M. Loktev, G. Vdovin, and L. Toporkova, Modal liquid crystal wavefront corrector, Opt. Express **10**, 1258 (2002).

[3] S. P. Kotova, P. Clark, I. R. Guralnik, N. A. Klimov, M. Y. Kvashnin, M. Y. Loktev, G. D. Love, A. F. Naumov, M. A. Rakhmatulin, C. D. Saunter, G. V. Vdovin, and O. A. Zayakin, Technology and electro-optical properties of modal liquid

crystal wavefront correctors, J. Opt. A: Pure Appl. Opt. **5**, S231 (2003).
[4] S. Xu, H. Ren, and S.-T. Wu, Adaptive liquid lens actuated by liquid crystal pistons, Opt. Express **20**, 28518 (2012).
[5] L. Hu, L. Xuan, Y. Liu, Z. Cao, D. Li, and Q. Mu, Phase-only liquid-crystal spatial light modulator for wave-front correction with high precision, Opt. Express **12**, 6403 (2004).
[6] I. Moreno, J. A. Davis, T. M. Hernandez, D. M. Cottrell, and D. Sand, Complete polarization control of light from a liquid crystal spatial light modulator, Opt. Express **20**, 364 (2012).
[7] *Spatial Light Modulator Technology: Materials, Applications, and Devices*, edited by U. Efron (Marcell Dekker, New York, 1995), p. 665.
[8] S. T. Lagerwall, *Ferroelectric and Antiferroelectric Liquid Crystals* (Wiley-VCH, New York, 1999), p. 427.
[9] P. Oswald and P. Pieranski, *Smectic and Columnar Liquid Crystals: Concepts and Physical Properies Illustrated by Experiments*, The Liquid Crystals Book Series (Taylor & Francis Group, London, 2006), p. 690.
[10] N. A. Clark and S. T. Lagerwall, Submicrosecond bistable electro-optic switching in liquid crystals, Appl. Phys. Lett. **36**, 899 (1980).
[11] L. A. Beresnev, V. G. Chigrinov, D. I. Dergachev, E. P. Poshidaev, J. Fünfschilling, and M. Schadt, Deformed helix ferroelectric liquid crystal display: A new electrooptic mode in ferroelectric chiral smectic C liquid crystals, Liq. Cryst. **5**, 1171 (1989).
[12] I. Abdulhalim and G. Moddel, Electrically and optically controlled light modulation and color switching using helix distortion of ferroelectric liquid crystals, Mol. Cryst. Liq. Cryst. **200**, 79 (1991).
[13] G. B. Cohen, R. Pogreb, K. Vinokur, and D. Davidov, Spatial light modulator based on a deformed-helix ferroelectric liquid crystal and a thin a-Si:H amorphous photoconductor, Appl. Opt. **36**, 455 (1997).
[14] E. Pozhidaev, S. Pikin, D. Ganzke, S. Shevtchenko, and W. Haase, High frequency and high voltage mode of deformed helix ferroelectric liquid crystals in a broad temperature range, Ferroelectrics **246**, 235 (2000).
[15] E. P. Pozhidaev, A. D. Kiselev, A. K. Srivastava, V. G. Chigrinov, H.-S. Kwok, and M. V. Minchenko, Orientational Kerr effect and phase modulation of light in deformed-helix ferroelectric liquid crystals with subwavelength pitch, Phys. Rev. E **87**, 052502 (2013).
[16] E. P. Pozhidaev, A. K. Srivastava, A. D. Kiselev, V. G. Chigrinov, V. V. Vashchenko, A. V. Krivoshey, M. V. Minchenko, and H.-S. Kwok, Enhanced orientational Kerr effect in vertically aligned deformed helix ferroelectric liquid crystals, Opt. Lett. **39**, 2900 (2014).
[17] E. Pozhidaev, V. Chigrinov, A. Murauski, V. Molkin, D. Tao, and H.-S. Kwok, V-shaped electro-optical mode based on deformed-helix ferroelectric liquid crystal with subwavelength pitch, J. Soc. Inf. Display **20**, 273 (2012).
[18] Z. Brodzeli, L. Silvestri, A. Michie, V. Chigrinov, Q. Guo, E. P. Pozhidaev, A. D. Kiselev, and F. Ladoucer, Liquid crystal-based hydrophone arrays, Photon. Sensors **2**, 237 (2012).
[19] Z. Brodzeli, L. Silvestri, A. Michie, Q. Guo, E. P. Pozhidaev, V. Chigrinov, and F. Ladouceur, Sensor at your fibre tips: a novel liquid crystal based photonic transducer for sensing systems, J. Lightwave Technol. **31**, 2940 (2013).
[20] A. D. Kiselev, E. P. Pozhidaev, V. G. Chigrinov, and H.-S. Kwok, Polarization-gratings approach to deformed-helix ferroelectric liquid crystals with subwavelength pitch, Phys. Rev. E **83**, 031703 (2011).
[21] A. D. Kiselev and V. G. Chigrinov, Optics of short-pitch deformed-helix ferroelectric liquid crystals: Symmetries, exceptional points, and polarization-resolved angular patterns, Phys. Rev. E **90**, 042504 (2014).
[22] J. N. McLeod, The axicon: A new type of optical elements, J. Opt. Soc. Am. **44**, 592 (1954).
[23] J. N. McLeod, Axicons and their uses, J. Opt. Soc. Am. **50**, 166 (1960).
[24] I. Manek, Y. B. Ovchinnikov, and R. Grimm, Generation of a hollow laser beam for atom trapping using an axicon, Opt. Commun. **147**, 67 (1998).
[25] P.-A Bélanger and M. Rioux, Ring pattern of a lens-axicon doublet illuminated by a Gaussian beam, Appl. Opt. **17**, 1080 (1978).
[26] S. Monk, J. Arlt, D. A. Robertson, J. Courtial, and M. J. Padgett, The generation of Bessel beams at millimetre-wave frequencies by use of an axicon, Opt. Commun. **170**, 213 (1999).
[27] J. Arlt and K. Dholakia, Generation of high-order Bessel beams by use of an axicon, Opt. Commun. **177**, 297 (2000).
[28] Y. Ismail, N. Khilo, V. Belyi, and A. Forbes, Shape invariant higher-order Bessel-like beams carrying orbital angular momentum, J. Opt. **14**, 085703 (2012).
[29] C. Snoeyink and S. Wereley, Single-image far-field sub-diffraction limit imaging with axicon, Opt. Lett. **38**, 625 (2013).
[30] J. Arlt, V. Garces-Chavez, W. Sibbett, and K. Dholakia, Optical micromanipulation using a Bessel light beam, Opt. Commun. **197**, 239 (2001).
[31] A. V. Korobtsov, S. P. Kotova, N. N. Losevskii, A. M. Maiorova, and S. A. Samagin, Formation of contour optical traps using a four-channel liquid crystal focusing device, Quantum Electron. **44**, 1157 (2014).
[32] R. Kampmann, A. K. Chall, R. Kleindienst, and S. Sinzinger, Optical system for trapping particles in air, Appl. Opt. **53**, 777 (2014).
[33] T. Carlsson, B. Žekš, C. Filipič, and A. Levstik, Theoretical model of the frequency and temperature dependence of the complex dielectric constant of ferroelectric liquid crystals near the smectic-C^* – smectic-A phase transition, Phys. Rev. A **42**, 877 (1990).
[34] B. Urbanc, B. Žekš, and T. Carlsson, Nonlinear effects in the dielectric response of ferroelectric liquid crystals, Ferroelectrics **113**, 219 (1991).
[35] P. Weinberger, John Kerr and his effects found in 1877 and 1878, Philos. Mag. Lett. **88**, 897 (2008).
[36] J. Yan, H.-C. Cheng, S. Gauza, Y. Li, M. Jiao, L. Rao, and S.-T. Wu, Extended Kerr effect of polymer-stabilized blue-phase liquid crystals, Appl. Phys. Lett. **96**, 071105 (2010).
[37] J. Yan, Z. Luo, S.-T. Wu, J.-W. Shiu, Y.-C. Lai, K.-L. Cheng, S.-H. Liu, P.-J. Hsieh, and Y.-C. Tsai, Low voltage and high contrast blue phase liquid crystal with red-shifted Bragg reflection, Appl. Phys. Lett. **102**, 011113 (2013).
[38] A. A. Zhukov, E. P. Pozhidaev, A. A. Bakulin, and G. P. Babaevski, Energy criteria for orientation of smectic C* liquid crystals in electrooptic elements, Crystallogr. Rep. **51**, 680 (2006).

[39] E. Pozhidaev, S. Torgova, M. Minchenko, C. A. R. Yednak, A. Strigazzi, and E. Miraldi, Phase modulation and ellipticity of the light transmitted through a smectic C^* layer with short helix pitch, Liq. Cryst. **37**, 1067 (2010).

[40] M. Born and E. Wolf, *Principles of Optics: Electromagnetic Theory of Propagation, Interference and Diffraction of Light*, 7th ed. (Cambridge University Press, New York, 1999), p. 952.

[41] A. D. Kiselev, Singularities in polarization resolved angular patterns: transmittance of nematic liquid crystal cells, J. Phys.: Condens. Matter **19**, 246102 (2007).

[42] A. D. Kiselev, R. G. Vovk, R. I. Egorov, and V. G. Chigrinov, Polarization-resolved angular patterns of nematic liquid crystal cells: Topological events driven by incident light polarization, Phys. Rev. A **78**, 033815 (2008).

[43] A. D. Rakić, A. B. Djurišić, J. M. Elazar, and M. L. Majewski, Optical properties of metallic films for vertical-cavity optoelectronic devices, Appl. Opt. **37**, 5271 (1998).

[44] J. W. Goodman, *Statistical Optics*, 2nd ed., Wiley Series for Pure and Applied Optics (Wiley, New York, 2015), p. 516.

[45] E. O. Brigham, *The Fast Fourier Transform and its Applications*, Prentice Hall Signal Processing Series (Prentice Hall, New Jersey, 1988), p. 448.

[46] E. Gorecka, A. D. L. Chandani, Y. Ouchi, H. Takezoe, and A. Fukuda, Molecular orientational structures in ferroelectric and antiferroelectric smectic liquid crystal phases as studied by conoscopic observation, Jpn. J. Appl. Phys. **29**, 131 (1990).

[47] J.-k. Song, A. D. L. Chandani, A. Fukuda, J. K. Vij, I. Kobayashi, and A. V. Emelyanenko, Temperature-induced sign reversal of biaxiality observed by conoscopy in some ferroelectric Sm-C^* liquid crystals, Phys. Rev. E **76**, 011709 (2007).

[48] J.-K. Song, J. K. Vji, and K. Sadashiva, Conoscopy of chiral smectic liquid crystal cells, J. Opt. Soc. Am. A **25**, 1820 (2008).

[49] T. P. Rieker, N. A. Clark, G. S. Smith, D. S. Parmar, E. B. Sirota, and C. R. Safinya, "Chevron" Local Layer Structure in Surface-Stabilized Ferroelectric Smectic-*C* Cells, Phys. Rev. Lett. **59**, 2658 (1987).

[50] J. Fünfshilling, M. Stalder, and M. Shadt, Photoaligned orientation layers for ferroelectric LCD's, Ferroelectrics **244**, 257 (2000).

[51] Y. Takanishi, Y. Ouchi, H. Takezoe, A. Fukuda, A. Mochizuki, and M. Nakatsuka, Spontaneous formation of quasi-bookshelf layer structure in new ferroelectric liquid crystals derived from a naphthalene ring, Jpn. J. Appl. Phys. Part 2 **29**, L984 (1990).

[52] A. Mochizuki, M. Hirose, M. Nakatsuka, and M. Toatsu, Zigzag defect free alignment and good bistability of surface stabilized S_c^* cells, Ferroelectrics **113**, 353 (1991).

[53] C. P. J. Schubert, A. Bogner, J. H. Porada, K. Ayub, T. Andrea, F. Giesselmann, and R. P. Lemieux, Design of liquid crystals with 'de Vrieslike' properties: carbosilane-terminated 5-phenylpyrimidine mesogens suitable for chevron-free FLC formulations, J. Mater. Chem. C **2**, 4581 (2014).

[54] E. G. Abramochkin, K. N. Afanas'ev, V. G. Volostnikov, A. V. Korobtsov, S. P. Kotova, N. N. Losevskii, A. M. Maiorova, and E. V. Razueva, Formation of vortex light fields of specified intensity for laser micromanipulation, Bull. Russ. Acad. Sci.: Phys. **72**, 68 (2008).

[55] A. D. Kiselev and R. G. Vovk, Structure of polarization-resolved conoscopic patterns of planar oriented liquid crystal cells, JETP **110**, 901 (2010).